

Lunar regolith and substructure at Chang'E-5 landing site in the northern Oceanus Procellarum

Hanjie Song

State Key Laboratory of Space Weather, National Space Science Center, Chinese Academy of Sciences

Hui Sun

Faculty of Geosciences and Environmental Engineering, Southwest Jiaotong University

Gang Yu

School of Electrical Engineering, University of Jinan

Yang Liu (✉ yangliu@nssc.ac.cn)

State Key Laboratory of Space Weather, National Space Science Center, Chinese Academy of Sciences

Juan Li

State Key Laboratory of Mineral Deposit Research, School of Earth Sciences and Engineering, Nanjing University

Menglong Xu

Institute of Geophysical and Geochemical Exploration, Chinese Academy of Geological Science

Yikang Zheng

Institute of Geology and Geophysics, Chinese Academy of Sciences

Chao Li

Institute of Geology and Geophysics, Chinese Academy of Sciences

Yong Pang

China Academy of Space Technology, Beijing spacecrafts

Guoxin Wang

China Academy of Space Technology, Beijing spacecrafts

Ping Zhao

School of Information Science and Engineering, Shandong Normal University

Yongliao Zou

State Key Laboratory of Space Weather, National Space Science Center, Chinese Academy of Sciences

Article

Keywords: lunar regolith, LRPR, radar, imaging, oceanus procellarum

Posted Date: September 23rd, 2021

DOI: <https://doi.org/10.21203/rs.3.rs-912528/v1>

License: © ⓘ This work is licensed under a Creative Commons Attribution 4.0 International License.

[Read Full License](#)

22 **Abstract**

23 **The Lunar Regolith Penetrating Radar (LRPR) on the Chang'E-5 (CE-5) lander was**
24 **deployed to investigate structures of the regolith. The migration and ridge detection**
25 **methods were used to process the radar data, and the results indicate a 4.5 m regolith**
26 **thickness that contains four units at the landing site, which is characterized by different**
27 **internal reflections that point to their various compositions, mainly comprise protolith and**
28 **admixed ejecta from the Harpalus, Copernicus, and Aristarchus. High-resolution**
29 **processing for the LRPR data indicates a few rocks or slates with depth from ~0.2 m to over**
30 **1 m in the subsurface at the landing site, which was validated by the force analysis during**
31 **the drilling of the regolith into ~1 m depth. The processing procedure proposed in this study**
32 **is capable of producing reliable and precise images of the lunar regolith substructure,**
33 **which provides important geological context on the returned drilling samples.**

34 **Introduction**

35 As China's first lunar sample-return mission, and the first lunar return mission of humanity
36 since Soviet Union's Luna 24 in 1976¹, Chang'E-5 (CE-5) was landed at 43.06°N, 51.92°W on the
37 1st December, 2020, which is close to the Mons Rümker, a volcano to the north of Oceanus
38 Procellarum^{2,3,4}. CE-5 brings back 1.731 kg regolith and fragmented rock samples composed of
39 the youngest mare basalts on the moon, which were formed at 1~2 Ga by crater population
40 studies³. The collected samples were postulated to form as results of young volcanism in the

41 landing area^{2,3,5}. The LRPR was one main payload of the lander for CE-5 and used to investigate
42 the shallow structures of the regolith with a 5 cm-scale of high detecting resolution^{6,7}.

43 The lunar surface is covered by regolith, which experienced continuous asteroid
44 bombardments and long-term volcanic eruptions since its formation⁸. Processes such as
45 bombardments and volcanic eruptions significantly deformed materials at the lunar surface, and
46 also complicated the subsurface structures, which contain important evidences for the Moon's
47 surface exploration⁹. Subsurface structures of the regolith preserve vital clues on the 4 Ga's lunar
48 history¹⁰. Thickness of the regolith was studied by *in-situ* drilling¹⁰, seismic experiments¹¹,
49 microwave remote sensing¹², impact crater morphology, and distribution of the crater diameters¹³,
50 which suggest a range of ~2 m beneath the young lunar maria to over 10 m beneath the lunar
51 highlands of the regolith^{9,14}. Unlike the Apollo Lunar Missions, which conducted Lunar Sounder
52 Experiments^{15,16}, the Chang'E-3 lunar mission conducted the first *in-situ* Lunar Penetrating Radar
53 (LPR) exploration with wide frequency bands and high spatial resolutions in the Imbrium basin,
54 which unraveled detailed structures of the lunar regolith^{8,17}. Results of the Chang'E-3 LPR data
55 indicate multi-layered ejecta in the Moon's regolith, and brecciated underlying bedrocks, which
56 significantly improves our understanding of surface evolution and volcanic eruption histories of
57 the Moon^{8,17}. Furthermore, the Chang'E-4 lunar mission conducted the first *in-situ* LPR
58 exploration and offered valuable information on the farside of the Moon in the Von Kármán
59 crater at the South Pole-Aitken basin^{9,18}. Based on early experiences of the LPR and earlier
60 planetary radars missions, the LRPR is designed to have *in-situ* operations with multi-
61 inputs/outputs asymmetric antenna arrays attached on the bottom of the CE-5 lander, which

62 includes 12 off-ground high-resolution Vivaldi antennas. Collected data of the LRPR were used
63 to analyses the lunar regolith structures in more details within a detecting depth of ~4.5 m and 5
64 cm-scale resolution, and to support further drilling and sampling missions⁷.

65 The CE-5 was landed in the northern Oceanus Procellarum (Fig. 1), with some of the
66 youngest mare basalts being discovered on the Moon¹. Drilling for the subsurface samples and
67 scooping for the surface samples have great potentials to improve our understandings of thermal
68 evolution and impact histories of the Moon¹⁹. Figure 2 presents the initial processed LRPR data,
69 which underwent decoding, denoising, background removal and data gaining processing.
70 Amplitudes of the electromagnetic waves are proportional to the dielectric constants of the lunar
71 regolith or rock contrasts, which are primarily influenced by their porosities and
72 compositions^{8,13,17}. Strong reflections occurred at boundaries between the regolith (fine-grained
73 soil dominated), the ejecta layer (rock clast dominated), the brecciated bedrock zones, and
74 bedrocks, and within the ejecta layer and the brecciated bedrock zones⁹. Weak reflections occur
75 within a few of scattered rock clasts while no reflection is observed in the fine-grained regolith
76 and homogeneous basalt layers^{9,20}. Further processing of the LRPR data, including Kirchhoff
77 migration²¹ with envelope processing, and ridge detection^{22,23} were conducted to enhance the
78 reliability of the depths and shapes of the reflectors (Fig. 3). The LRPR data addressed by
79 bandpass filtering and ridge detection methods were then used to analyze the migration results
80 and to obtain reliable stratigraphic subdivision results, which helped to expound material
81 composition sources at the CE-5 landing site (Fig. 4).

82 **Results**

83 Figure 3a shows the processed LRPR data using the Kirchhoff migration²¹ and Figure 3b
84 shows the LRPR data generated from ridge detection method^{22,23}, which unravel the thickness and
85 structures of the lunar regolith with higher-resolution. According to stratigraphic analysis at the
86 CE-5 landing site, pre-mare basalt materials consist of ancient highland materials including
87 Procellarum KREEP Terrane crust, ejecta from Iridum Basin, and local silica-rich volcanic³.
88 Although the ray and secondary crater deposits in the regolith contain important exotic ejecta, the
89 actual deposits at the CE-5 landing site are still dominated by local materials^{24,25}. The
90 substructure at the CE5 landing site can be divided into four stratigraphic units according to the
91 amplitude/energy distribution of the reflections as: strong reflection, sub-strong reflection, weak
92 reflection and subtle reflection units from top to bottom (unit A to D). Length and tilt direction of
93 the ridges in Fig. 3b reflect the sizes and arrangement modes of the fragmented rocks, which
94 indicate that units A and C are mainly composed of disordered fragmented rocks. Number of
95 fragmented rocks in units B and C decrease with increasing burial depths. With further increasing
96 depths, rock sizes in unit D are much larger and the reflecting surface is more flattened.

97 The bottom unit D is over 1 m thick, and shows subtle reflection inside, suggesting relatively
98 homogeneous compositions of this layer. Thus, unit D could be deciphered as the basalt bedrock
99 (Fig. 5), which is postulated to form by the youngest mare volcanism in the landing area²⁴. The
100 weak reflection unit (unit C), with a thickness of ~1.3 m, lies directly on the mare basalt unit (unit
101 D), shows few internal and holonomic reflectors, is inferred as a transition zone containing rock
102 breccia/fractured basalts (Fig. 3). During the accumulation of the ejecta layer, coherent mare

103 basalt at the base of was fractured, but not excavated, resulting in the formation of the proposed
104 transition zone. The sub-strong reflection unit (unit B), with a thickness of ~1.0 m, shows a small
105 number of observed reflectors, indicating rocks originated from crater ejecta. The strong
106 reflection unit (unit A), with a thickness of ~1.5 m, shows abundant and cluttered reflections
107 when compared with that of the lower unit B (Fig. 3), suggesting abundant rock boulders, which
108 were likely originated from the admixed ejecta.

109 According to the geological and stratigraphic analysis at the landing site, the admixed ejecta
110 of unit A were mainly originated from the Harpalus, Copernicus and Aristarchus³ (Fig. 5), with
111 few from the Sharp B, Mairan, and Harding craters (Fig. 1). This ejecta unit shows complex
112 internal structures, which is further divided into three sublayers (Fig. 4a~d). The top sub-layer is
113 ~0.2 m thick, shows homogeneous with fewer scatters, probably indicating fine-grained materials
114 with a scarcity of rock boulders, and hence is deciphered as fine-grained regolith. The middle
115 sublayer is characterized by strong reflections with a thickness of ~1 m, suggesting large sizes of
116 rock boulders or fragments (~10 cm, Fig. 4e and Fig. 4f). The bottom sublayer is ~0.3 m thick
117 and shows obvious weak reflections and indicates few rock fragments when compared with the
118 middle sublayer. The LRPR data reveal that multiple and episodic crater ejecta with increasing
119 intensity occurred at the landing site from unit B to A. The fragment rocks and soil distribute
120 randomly, resulting in the irregular shallow subsurface structures, which offers evidence that
121 young volcanism plays an important role in the formation of the lunar subsurface structures.
122 Detailed structures of the topmost ~2.7 m (Unit A and B) as revealed by the processed LRPR data
123 analysis are consistent with the drilling outcomes.

124 The processing procedures of the LRPR data were proved reliable to reveal the lunar regolith
125 subsurface structures by drilling processes of the CE-5 mission. The analyses of LRPR data show
126 a strong reflection at a depth of ~ 0.75 m, which is postulated to be fragmented rocks (Fig. 4a).
127 The drilling mission verified that rock fragments occurred at a depth of 0.753 m, which leads to
128 the dramatic increase of pulling force while drilling (Figs. 4a and 4b). Figure 4a also reveals
129 several large force feedback positions (orange arrow), which are highly consistent with the
130 Kirchhoff migration and ridge detection results. The well correlation between our LRPR data
131 analysis and the drilling results strengthens our structural analysis of the lunar regolith and
132 verified that processing procedures in this research are reliable.

133 **Discussion**

134 Our LRPR data analyses indicate that shallow structures to the north of the Oceanus
135 Procellarum on the Moon's nearside are dominated by large-scale ejecta and surface regolith. The
136 well-defined subsurface structures are consistent with expectations of shallow structures in the
137 lunar upper crust^{25,26}, supporting the idea that the youngest volcanisms have significant effects on
138 the formation of lunar subsurface structures^{3,25,27}. The regolith and fragmented rock samples
139 collected by CE-5 comprise some of the youngest mare basalts on the moon, which are postulated
140 to form from the young volcanisms¹⁹. Our results improve the understandings of lunar thermal
141 evolution and impact histories. LRPR data analyses indicate that the shallow subsurface
142 structures were formed and influenced greatly by impact bombardments, that the shallow
143 subsurface were deformed. The Kirchhoff migration and ridge detection method provide reliable

144 methods to analyses subsurface structures, which can also be adopted to support future landing-
145 site selection, especially for future sample-return missions.

146 **Methods**

147 **Brief introduction of the LRPR.**

148 The LRPR is one of the main payloads on the CE-5 lander, which was deployed to detect
149 lunar regolith thickness and subsurface structures at the landing site to support the drilling and
150 sampling tasks^{7,25}. The LRPR is a time-domain carrier-free picoseconds impulse surface
151 penetrating radar with a Full Width at Half Maximum (FWHM) of 200 ps, which is 90 cm from
152 the lunar surface and operates with frequency ranges of 1~3 GHz⁷. The LRPR was operated *in-*
153 *situ* under static status, with one antenna sending pulse signals and 11 antennas receiving echo
154 signals. The 12 antennas produced 132 traces of data in one operation period, and each trace has a
155 time window of ~55 ns with a temporal sampling interval of 18.3 ps⁶. Interior structures of the
156 lunar regolith and other subsurface structures were analyzed by the electromagnetic waves
157 reflected from the subsurface. Electromagnetic waves are determined mainly by compositions
158 (for example, FeO and TiO₂ contents, see Fig. 5) and porosities of the regolith and other
159 subsurface materials based on the multi-offset migration results, that the LRPR could be
160 effectively used to detect the boundaries between the porous lunar regolith, ejecta, basalt lava
161 layers, and bedrock. The lunar regolith and ejecta layers often contain large rock boulders (larger
162 than the spatial resolution of the radar wave), that signals reflected by the interfaces of these large
163 boulders were detected⁸.

164 The LRPR is installed at the bottom of one edge of the lander, which consists of 12 separate
165 antennas with a center working frequency of 2 GHz. Intervals of the array #1~10 is 12 cm and the
166 distance between antenna #7 and #8 is 58.45 cm. Antenna #11 is in the same plane as antennas
167 #1~10, which is ~90 cm from the lunar surface, and 12 cm from antenna #8. Antenna #12 is
168 installed by the side of the lander, which is 16.75 cm, 5.24 cm, and ~107.25 cm from the planes
169 of antennas #1~10, antenna #7 and the lunar surface, respectively. The longest dimension of the
170 antenna array provides a synthetic aperture of ~1.554 m and the diameter of the drill pipe is 3.27
171 cm.

172 **Preprocessing of the LRPR data.**

173 The original 132 traces of LRPR data were sequenced according to the antenna offsets are
174 shown in Fig. 6a. Pre-processing procedures for the LRPR traces consist of DC removal, cable
175 delay correction, and background removal. We apply a sixth-order Butterworth bandpass filter
176 between 1 and 3 GHz on each trace and remove the background (Fig. 6b). Fig. 6c shows that
177 background removal has a great influence on LRPR data preprocessing.

178 **Introduction of the Kirchhoff migration.**

179 Migration technology is an important wavefield signal processing method, which is essential
180 for extracting weak signals to produce high-accuracy images of subsurface structures^{28,29}.
181 Migration methods are widely used in seismic exploration and different migration methods were
182 developed to meet different exploration needs. Since the electrical field component of the
183 electromagnetic wave is also consistent with scalar wave equation, many seismic migration
184 methods can be applied to electromagnetic wave signal processing. Migration methods had been

185 applied to process the LPR data from the Chang'E-3 and Chang'E-4 missions^{8,9}, which verified
 186 that migration methods are effective and applicable for high-resolution imaging of the complex
 187 subsurface structures and objects in the lunar regolith.

188 Seismic migration methods are divided into different types according to various
 189 implementation methods, such as Kirchhoff migration³⁰, Stolt migration (or f-k migration)³¹,
 190 phase-shift migration³² and reverse time migration^{33,34}. Among these methods, Kirchhoff
 191 migration is a stable and fast migration algorithm²¹, which is less dependent on the migration
 192 model, and has strong adaptability. In addition, Kirchhoff migration is flexible, which is able to
 193 meet processing requirements of irregular observation systems³⁵. Considering that the advantages
 194 of Kirchhoff migration are consistent with the characteristics of LRPR data, we used this method
 195 for imaging the structures of lunar regolith.

196 The theoretical basis of high-frequency electromagnetic wave Kirchhoff migration is to
 197 solve the electric field $E(x, y, z; t)$ that satisfies the scalar wave equation through the integration
 198 method³⁶

$$199 \quad \frac{\partial^2 E}{\partial x^2} + \frac{\partial^2 E}{\partial y^2} + \frac{\partial^2 E}{\partial z^2} = \frac{1}{v} \frac{\partial^2 E}{\partial t^2},$$

200 where x , y , z represent spatial coordinates and t represents time coordinate; v is the
 201 electromagnetic wave velocity. The Kirchhoff integral solution of the wave equation at point
 202 (x_0, y_0, z_0) have two solutions: the upgoing wavefield and the downgoing wavefield. For the
 203 upgoing wavefield

$$204 \quad E_{up}(x_0, y_0, z_0; t) = \frac{1}{2\pi} \iint_{\Omega} \left[\frac{\partial}{\partial z} \left(\frac{1}{r} \right) - \frac{1}{vr} \frac{\partial r}{\partial z} \frac{\partial}{\partial z} \right] E \left(x, y, z; t - \frac{r}{v} \right) d\Omega,$$

205 and for the downgoing wavefield

206
$$E_{down}(x_0, y_0, z_0; t) = \frac{1}{2\pi} \iint_{\Omega} \left[\frac{\partial}{\partial z} \left(\frac{1}{r} \right) - \frac{1}{vr} \frac{\partial r}{\partial z} \frac{\partial}{\partial z} \right] E \left(x, y, z; t + \frac{r}{v} \right) d\Omega,$$

207 where Ω is the set of points on the surface, r is the distance from point (x_0, y_0, z_0) to the point of
 208 Ω . According to the exploding source principle²⁸, when t is equal to 0, the electric field
 209 represents the imaging result. Therefore, the Kirchhoff migration formula is

210
$$E(x_0, y_0, z_0; 0) = \frac{1}{2\pi} \iint_{\Omega} \left[\frac{\partial}{\partial z} \left(\frac{1}{r} \right) - \frac{1}{vr} \frac{\partial r}{\partial z} \frac{\partial}{\partial z} \right] E \left(x, y, 0; \frac{2r}{v} \right) d\Omega,$$

211 where $E \left(x, y, 0; \frac{2r}{v} \right)$ represents the received electromagnetic wave signal.

212 **Introduction of the ridge detection method.**

213 Ricker wave pulse signals are created and radiated to the lunar regolith through antennas of the
 214 LRPR. Images of the lunar regolith thickness and structures can then be generated according to
 215 the backward travelling waves from the spots or interfaces. Travel time of the electromagnetic
 216 waves has important effect on high-resolution imaging. To improve imaging quality of the lunar
 217 regolith and substructure, it is key to derive accurate arrival time of the backward electromagnetic
 218 waves³⁷. Time-frequency analysis (TFA) methods, e.g., short-time Fourier transform (STFT) and
 219 continuous wavelet transform, are designed to expand the time-series signals to two-dimensional
 220 time-frequency domain³⁸. The joint time-frequency characteristics can be extracted from
 221 conventional time-frequency representation. However, conventional methods often have
 222 difficulty to achieve the best resolution simultaneously in both time and frequency due to the
 223 Heisenberg-Gabor uncertainties, which implies that it is impossible to extract the precise time
 224 information from the representation generated by conventional methods alone. To overcome this
 225 limitation, this study presents a post-processing technology to extract the precise arrival time of
 226 the backward electromagnetic waves, which benefits high-resolution imaging in this study.

227 The Fig. 7a and 7c show the waveform and frequency spectrum of a simulated Ricker wave
 228 at the time instant 0 s, and the central frequency of the signal is 10 Hz. The STFT is used to
 229 generate the time-frequency representation of the signal (Fig. 7b). Results show that the time-
 230 frequency characteristic has a highly smeared distribution in both time and frequency directions.
 231 For an impulse-like signal^{22,39}, it can be modeled from the following frequency expression

$$232 \quad \hat{s}(\omega) = A(\omega)e^{i\varphi(\omega)},$$

233 where $\hat{s}(\omega)$ denotes the Fourier transform of the signal, $A(\omega)$ and $\varphi(\omega)$ are the signal
 234 amplitude and phase in frequency domain, and $-\varphi'(\omega)$ is a group delay (GD) parameter. The GD
 235 can be used to determine the arrival time instant of the signals for each frequency point²².
 236 However, it is necessary to improve the energy concentration of the time-frequency
 237 representation to obtain higher accuracies. Recent studies indicate that the GD can be regarded as
 238 the ridges of the STFT along the frequency direction^{22,23}, implying that it is possible to estimate
 239 the GD from the ridges of the time-frequency representation created by STFT. To obtain the
 240 STFT of the signal $\hat{s}(\omega)$, a local frequency model is needed and written as

$$241 \quad \hat{s}(\xi) = A(\omega)e^{i[\varphi(\omega)+\varphi'(\omega)(\xi-\omega)]},$$

242 where $\exists \varepsilon$ is assumed to be sufficiently small, $|A'(\omega)| \leq \varepsilon$ and $|\varphi''(\omega)| \leq \varepsilon$ for $\forall \omega$. Substituting
 243 this model into STFT, we derive

$$244 \quad \begin{aligned} G(t, \omega) &= (2\pi)^{-1} \int_{-\infty}^{+\infty} \hat{s}(\xi) \hat{g}(\xi - \omega) e^{i(\xi - \omega)t} d\xi \\ &= A(\omega) e^{i\varphi(\omega)} g(t + \varphi'(\omega)), \end{aligned}$$

245 where $g(\cdot)$ is the sliding even window function $\text{supp}(g) \in [-\Delta, \Delta]$, and $\hat{g}(\cdot)$ denotes the Fourier
 246 transform of the window function. The spectrogram of the signal can be obtained as

247 $|G(t, \omega)| = A(\omega)g(t + \varphi'(\omega)),$

248 It is known from this equation that the time-frequency energy of the signal has a large
249 distribution along the GD trajectory. Amplitude of the spectrogram reaches the maximum along
250 the GD trajectory for each frequency point. This inspires that the GD trajectory can be estimated
251 using the ridge detection method when the following two expressions $\partial|G(t, \omega)|/\partial t = 0$ and
252 $\partial^2|G(t, \omega)|/\partial t^2 < 0$ are satisfied at the same time^{40,41,42}.

253 To improve the energy concentration, spectrogram in the GD trajectory is retained and other
254 coefficients are removed as shown in Fig. 8a. The new time-frequency representation only
255 appears at the GD trajectory when compared to the large spread of the STFT spectrogram. The
256 slice of the new representation at the central frequency is then used to determine the precise time
257 instant when the impulse signal appears (Fig. 8b). Central frequency of the time-frequency
258 representation can be detected using the following expression

259
$$\omega_c = \arg \max_{\omega} \left(\int_{-\infty}^{+\infty} |G(t, \omega)| dt \right).$$

260 The slice at the central frequency can then be used to generate higher-resolution images of
261 the lunar regolith thickness and structures than that of the original time-series waveform of the
262 backward electromagnetic waves. In Fig. 9, a simulated time-series signal of four Ricker waves is
263 used to further confirm the effectiveness of the proposed method.

264 **Validation of the geological interpretation.**

265 Based on LPRP data analysis, four units with different compositions were classified in this
266 study.

267 Unit D is characterized with subtle reflections, indicating that the mare basalt is
268 homogeneous, with few fragments being developed. The landing site is near Mons Rümker in the
269 north of the Oceanus Procellarum basin, which is filled with Eratosthenian mare material in the
270 Procellarum KREEP Terrane³. The mare basalts were dated to be younger than 1.6 Ga^{5,19,24,25,43},
271 and are characterized with significant-high FeO and TiO₂ contents (see Fig. 5)^{19,24,25}. The average
272 accumulation rate of regolith is ~5 mm per year and the thickness of regolith at CE-5 landing site
273 was estimated up to ~7 m and ~99% is over 2 m²⁵. The top surface of the mare basalt is identified
274 as 3.5 m in our analyses, which corresponds to the accumulation processing.

275 Units C~A comprise materials of the lunar regolith deposited since Copernican, which were
276 produced by continuous impacting and space weathering processes^{10,25,44}. Unit C is defined as a
277 transition zone with disordered blocks being observed, which were marked by the weak
278 reflections as shown by the LPRP data analysis (Fig. 3). Unit C was formed by intensive and long
279 ejecta processes on the mare basalt, resulting in the development of fragmented rocks. The soil
280 was developed in unit C were originated from the mare basalt.

281 Materials in unit B were Imbrium-aged and Eratosthenian-aged mare basalts, highlands, and
282 impact crater materials, which were postulated to be originated from local materials, admixed
283 ejecta and exotic materials²⁵. Local materials were characterized with high TiO₂ contents, that
284 materials of low TiO₂ contents were inferred to source from distal ejecta²⁵. Potential ejecta
285 sources include the Aristarchus, Aristoteles, Langrenus, Harpalus, Copernicus, Sharp B, Harding,
286 Robertson craters, and Pythagoras, Philolaus, Hausen craters above 60 degrees⁴⁵. Considering
287 ages, distribution distances, sizes of the potential impact craters, and the thicknesses and

288 compositions of craters around the landing site, the Harpalus, Copernicus, and Aristarchus craters
289 with Copernicus ages may have the most significant contributions to the existence of admixed
290 ejecta at the landing site²⁵. Unit B is developed during the initial stage of impact cratering, which
291 shows sub-high reflections on LPRP data due to the significant difference between unit C and
292 unit B in terms of physical properties, size grading, and arrangement modes of materials in these
293 two units.

294 Unit A, which is correspondent to high reflections, shows randomly distributed blocks on the
295 LPRP data. During the development of unit A, more intensive impact ejecta processes occurred
296 first that massive structures were observed, which were followed by space weathering processes.
297 Fine-grained regolith is developing, which is characterized by relatively weak reflections when
298 compared to that of the lower part.

299 **References**

- 300 1. Liu, J. J. et al. Landing Site Selection and Overview of China's Lunar Landing Missions.
301 *Space Sci. Rev.* **217**, 6 (2021).
- 302 2. Qiao, L. et al. Geology of the Chang'e-5 landing site: Constraints on the sources of samples
303 returned from a young nearside mare. *Icarus* **364**, 114480 (2021).
- 304 3. Qian, Y. Q. et al. Young lunar mare basalts in the Chang'e-5 sample return region, northern
305 Oceanus Procellarum. *Earth Planet. Sci. Lett.* **555**, 116702 (2020).
- 306 4. Wang, J. et al. Localization of the Chang'e-5 Lander Using Radio-Tracking and Image-
307 Based Methods. *Remote Sens.* **13**, 590 (2021).

- 308 5. Hiesinger H. et al. Ages and stratigraphy of lunar mare basalts: A synthesis. *Spec. Pap. Geol.*
309 *Soc. Am.* **477**, 1–51 (2011).
- 310 6. Feng, J. Q. et al. An imaging method for Chang'e-5 Lunar Regolith Penetrating Radar.
311 *Planet. Space Sci.* **167**, 9–16 (2019).
- 312 7. Li, Y. X. et al. The Imaging Method and Verification Experiment of Chang'E-5 Lunar
313 Regolith Penetrating Array Radar. *IEEE Geosci. Remote. Sens. Lett.* **99**, 1–5 (2018).
- 314 8. Zhang, J. H. et al. Volcanic history of the Imbrium basin: A close-up view from the lunar
315 rover Yutu. *Proc. Natl. Acad. Sci.* **112**, 5342–5347 (2015).
- 316 9. Zhang, J. H. et al. Lunar regolith and substructure at Chang'E-4 landing site in South Pole-
317 Aitken basin. *Nat. Astron.* **5**, 1–6 (2021).
- 318 10. Heiken, G. H., Vaniman, D. T. & French, B. M. *Lunar sourcebook: A user's guide to the*
319 *Moon*: The University of Cambridge (1991).
- 320 11. Nakamura, Y. et al. Apollo Lunar Seismic Experiment—Final summary. *J. Geophys. Res.*
321 *Space Phys.* **87**, A117–A123 (1982).
- 322 12. Fa, W. Z. & Jin, Y. Q. A primary analysis of microwave brightness temperature of lunar
323 surface from Chang-E 1 multi-channel radiometer observation and inversion of regolith layer
324 thickness. *Icarus*, **207**, 605–615 (2010).
- 325 13. Neish, C. D. et al. Spectral properties of titan's impact craters imply chemical weathering of
326 its surface. *Geophys. Res. Lett.* **42**, 3746–3754 (2015).
- 327 14. Montopoli, M. et al. Remote sensing of the Moon's subsurface with multifrequency
328 microwave radiometers: A numerical study. *Radio Science* **46**, 1–13 (2011).

- 329 15. Porcello, L. et al. The Apollo lunar sounder radar system. *Proc. IEEE* **62**, 769–783 (1974).
- 330 16. Ono, T. et al. The Lunar Radar Sounder (LRS) Onboard the KAGUYA (SELENE)
331 Spacecraft. *Space Sci. Rev.* **154**, 145–192 (2010).
- 332 17. Xiao, L. et al. A young multilayered terrane of the northern Mare Imbrium revealed by
333 Chang'E-3 mission. *Science* **347**, 1226–1229 (2015).
- 334 18. Li, C. L. et al. The Moon's farside shallow subsurface structure unveiled by Chang'E-4
335 Lunar Penetrating Radar. *Sci. Adv.* **6**, eaay6898 (2020).
- 336 19. Qian, Y. Q. et al. The Long Sinuous Rille System in Northern Oceanus Procellarum and Its
337 Relation to the Chang'e-5 Returned Samples. *Geophys. Res. Lett.* **48**, 11 (2021).
- 338 20. Lv, W. M. et al. Comparative analysis of reflection characteristics of lunar penetrating radar
339 data using numerical simulations. *Icarus* **350**, 113896 (2020).
- 340 21. Docherty, P. A brief comparison of some Kirchhoff integral formulas for migration and
341 inversion. *Geophysics* **56**: 1164–1169 (1991).
- 342 22. Yu, G. & Lin, T. R. Second-order transient-extracting transform for the analysis of
343 impulsive-like signals. *Mech. Syst. Signal Process.* **147**, 107069 (2021).
- 344 23. Yu, G. A concentrated time–frequency analysis tool for bearing fault diagnosis. *IEEE Trans.*
345 *Instrum. Meas.* **69**, 371–381 (2019).
- 346 24. Qian, Y. Q. et al. Geology and Scientific Significance of the Rümker Region in Northern
347 Oceanus Procellarum: China's Chang'E-5 Landing Region. *J. Geophys. Res. Planets* **123**,
348 1407–1430 (2018).

- 349 25. Qian, Y. Q. et al. China's Chang'e-5 landing site: Geology, stratigraphy, and provenance of
350 materials. *Earth Planet. Sci. Lett.* **561**, 116855 (2021).
- 351 26. McGetchin, T. R. et al. Radial thickness variation in impact crater ejecta: implications for
352 lunar basin deposits. *Earth Planet. Sci. Lett.* **20**, 226–236 (1973).
- 353 27. Zhang, F. et al. The lunar mare ring-moat dome structure (RMDS) age conundrum:
354 Contemporaneous with Imbrian-aged host lava flows or emplaced in the Copernican?. *J.*
355 *Geophys. Res. Planets* **126**, e2021JE006880 (2021).
- 356 28. Claerbout, J. F. *Imaging the Earth's Interior*: Blackwell Scientific (1985).
- 357 29. Yilmaz, Ö. *Seismic Data Processing*: Society of Exploration Geophysicists (1987).
- 358 30. Schneider, W. A. Integral formulation for migration in two and three dimensions.
359 *Geophysics* **43**, 49–76 (1978).
- 360 31. Stolt, R. Migration by fourier transform. *Geophysics* **43**, 23–48 (1978).
- 361 32. Gazdag, J. Wave equation migration with the phase-shift method. *Geophysics* **43**, 1342–1351
362 (1978).
- 363 33. Baysal, E. et al. Reverse time migration. *Geophysics* **48**, 1514–1524 (1983).
- 364 34. Liu, H. et al. Two-Dimensional Reverse-Time Migration Applied to GPR with a 3-D-to-2-D
365 Data Conversion. *IEEE J. Sel. Top. Appl. Earth Obs. Remote Sens.* **10**, 4313–4320 (2017).
- 366 35. Jäger, C. et al. True-amplitude Kirchhoff migration from topography. *SEG Technical*
367 *Program Expanded Abstracts* **22**: 909–912 (2003).
- 368 36. Roberts, R. L. & Daniels, J. J. Modeling near-field GPR in three dimensions using the FDTD
369 method. *Geophysics* **62**, 1114–1126 (1997).

- 370 37. Morlet, J. et al. Wave propagation and sampling theory—Part I: complex signal and scattering
371 in multilayered media. *Geophysics* **47**, 203–221 (1982).
- 372 38. Mallat, S. A. *Wavelet Tour of Signal Processing: The Sparse Way*: Academic Press (2008).
- 373 39. Boashash, B. *Time-Frequency Signal Analysis and Processing: A Comprehensive Reference*:
374 Academic Press (2015).
- 375 40. Delprat, N. et al. Asymptotic wavelet and Gabor analysis: extraction of instantaneous
376 frequencies. *IEEE Trans. Inf. Theory* **38**, 644–664 (1992).
- 377 41. Carmona, R. A. et al. Characterization of signals by the ridges of their wavelet transforms.
378 *IEEE Trans. Signal Process.* **45**, 2586–2590 (1997).
- 379 42. Stanković, L. et al. Instantaneous frequency in time–frequency analysis: Enhanced concepts
380 and performance of estimation algorithms. *Digital Signal Process.* **35**, 1–13 (2014).
- 381 43. Wu, B. et al. Rock abundance and crater density in the candidate Chang’E-5 landing region
382 on the Moon. *J. Geophys. Res. Planets* **123**, 3256–3272 (2018).
- 383 44. Head, J.W. et al. Rethinking lunar mare basalt regolith formation: new concepts of lava flow
384 protolith and evolution of regolith thickness and internal structure. *Geophys. Res. Lett.* **47**,
385 e2020GL088334. (2020).
- 386 45. Xie, Y. Q. et al. The provenance of regolith at the Chang’e-5 candidate landing region. *J.*
387 *Geophys. Res. Planets* **125**, 2019JE006112 (2020).

388 **Data availability**

389 The data used in this work is available on the Science and Application Center for Moon and Deep
390 Space Exploration, Chinese Academy of Sciences (<http://moon.bao.ac.cn>).

391 **Code availability**

392 The code for processing the LRPR data is available from the corresponding author upon
393 reasonable request.

394 **Acknowledgments**

395 The CE-5 mission was carried out by the Chinese Lunar Exploration Program, and the data were
396 provided by the China National Space Administration and National Astronomical Observatory,
397 Chinese Academy of Sciences. This research was funded by the National Key R&D Program of
398 China (grant number: 2020YFE0202100), the National Natural Science Foundation of China
399 (grant number: 11941001), the pre-research project on Civil Aerospace Technologies funded by
400 Chinese National Space Administration (CNSA) (grant number: D020201 and D020203).

401 **Author contribution**

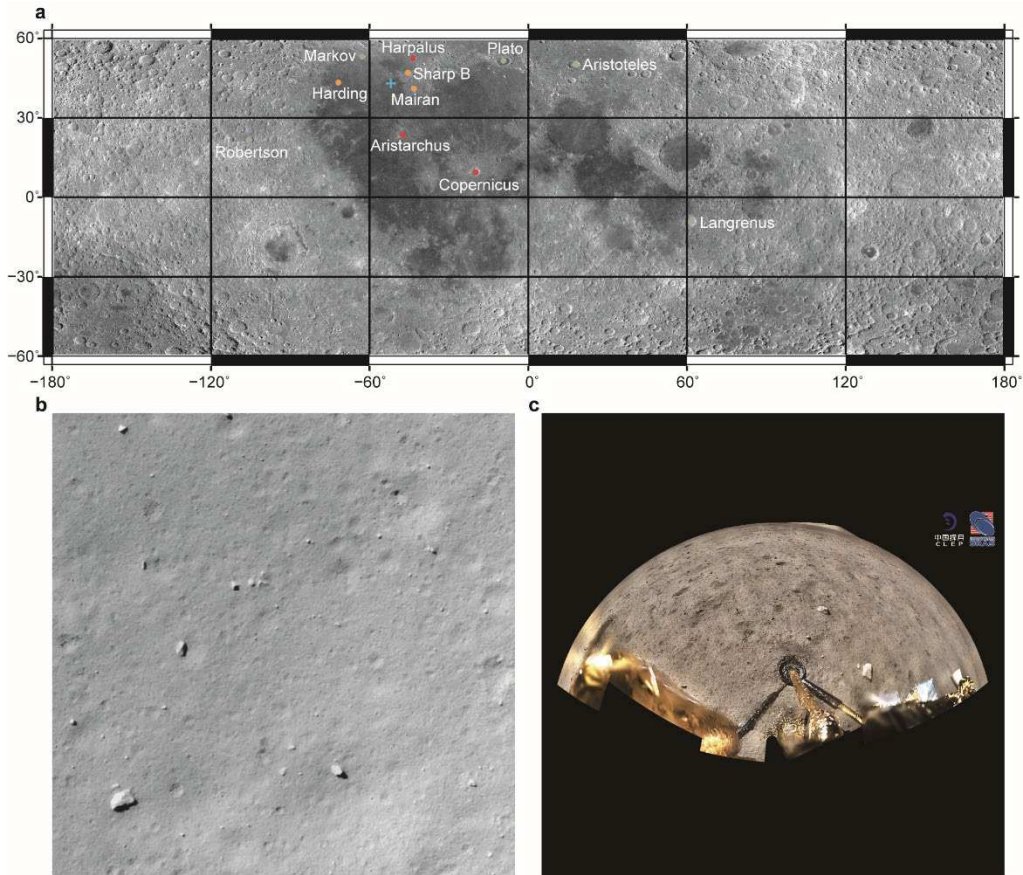
402 Y. L. and H.J.S. conceived and designed the experiments; H.J.S., H.S., G.Y., Y.Z., C.L. and P.Z.
403 performed the experiments and analyzed the data; H.J.S., J.L., M.X., A.Z., X.W., Y.P. and Y.L.Z.
404 interpreted the lunar geology; H.S. and Y.Z. implemented migration; G.Y. and P.Z. implemented
405 time-frequency division; H.J.S., H.S., G.Y., J.L. and M.X. wrote the paper.

406 **Competing interests**

407 The authors declare no competing interests.

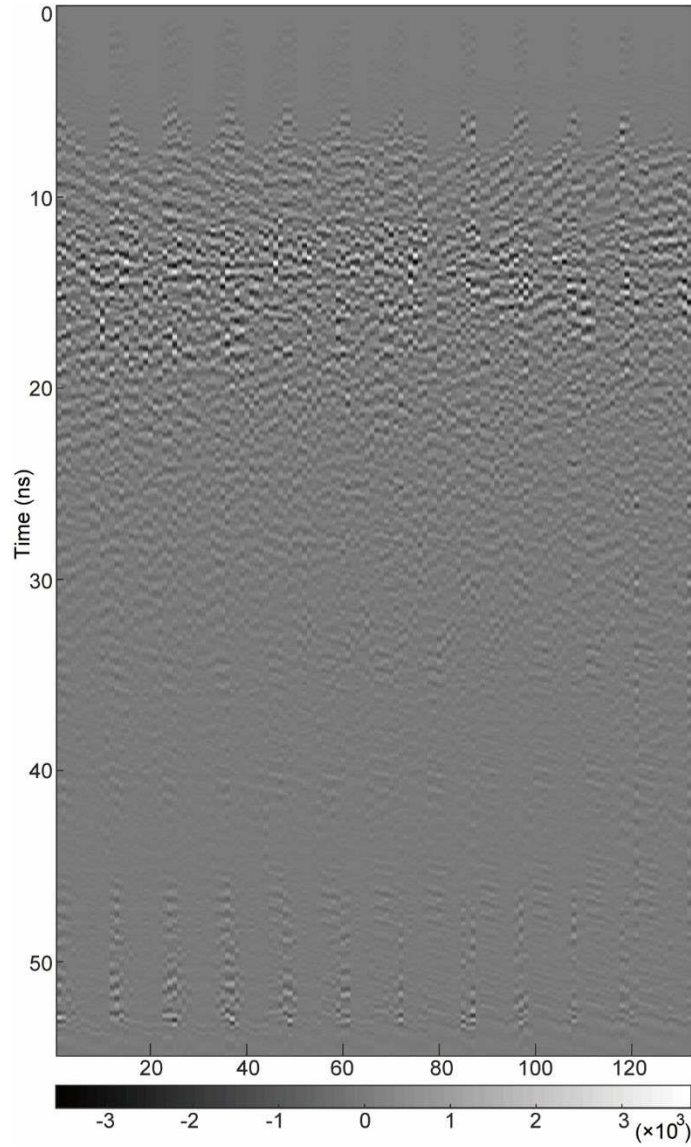
408 **Additional information**

409 Correspondence and requests for materials should be addressed to Y. L.



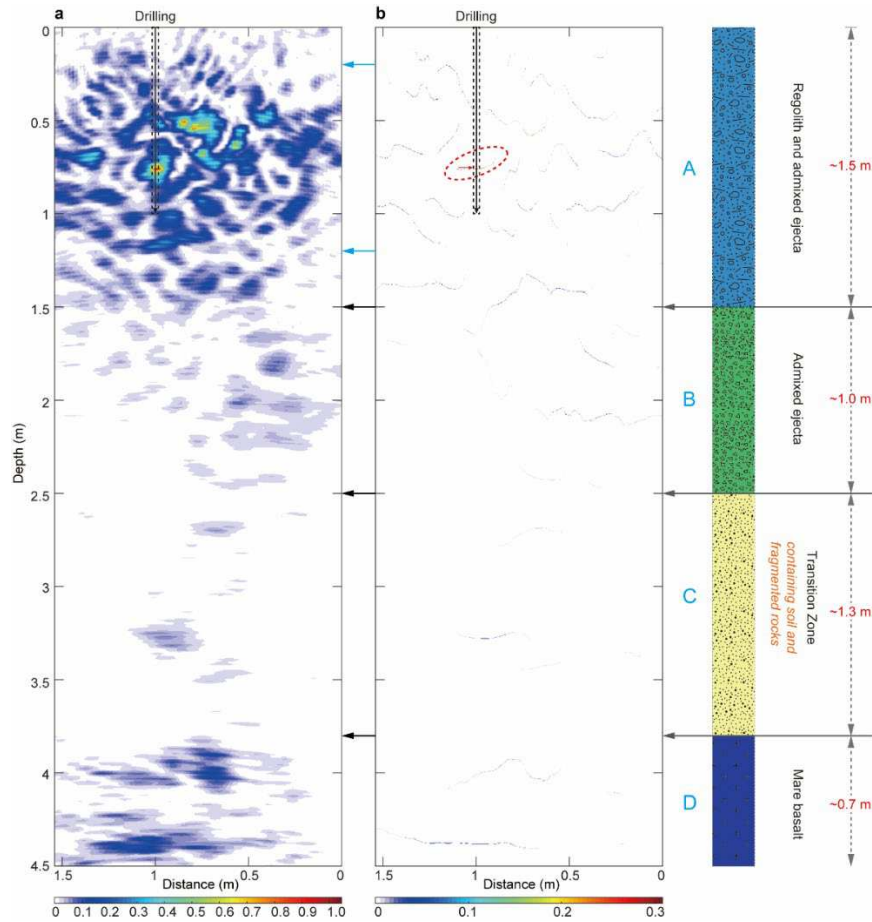
410

411 **Fig. 1 Location of the CE-5 landing site. a** The location of the CE-5 landing site is at the
 412 nearside of the Moon (blue cross). The background map is obtained by Chang'E-2
 413 (<http://moon.bao.ac.cn>). Materials origins in the study area mainly include the Copernicus,
 414 Aristarchus, and Harpalus craters (red dot), with scarce secondary materials from the Sharp B,
 415 Mairan, and Harding craters (orange dot). Other materials origins in the area may include the
 416 Markov, Plato, etc. (green dot). **b** Photo taking by the camera under the CE-5 lander during
 417 descending. **c** Panoramic image at the landing site.



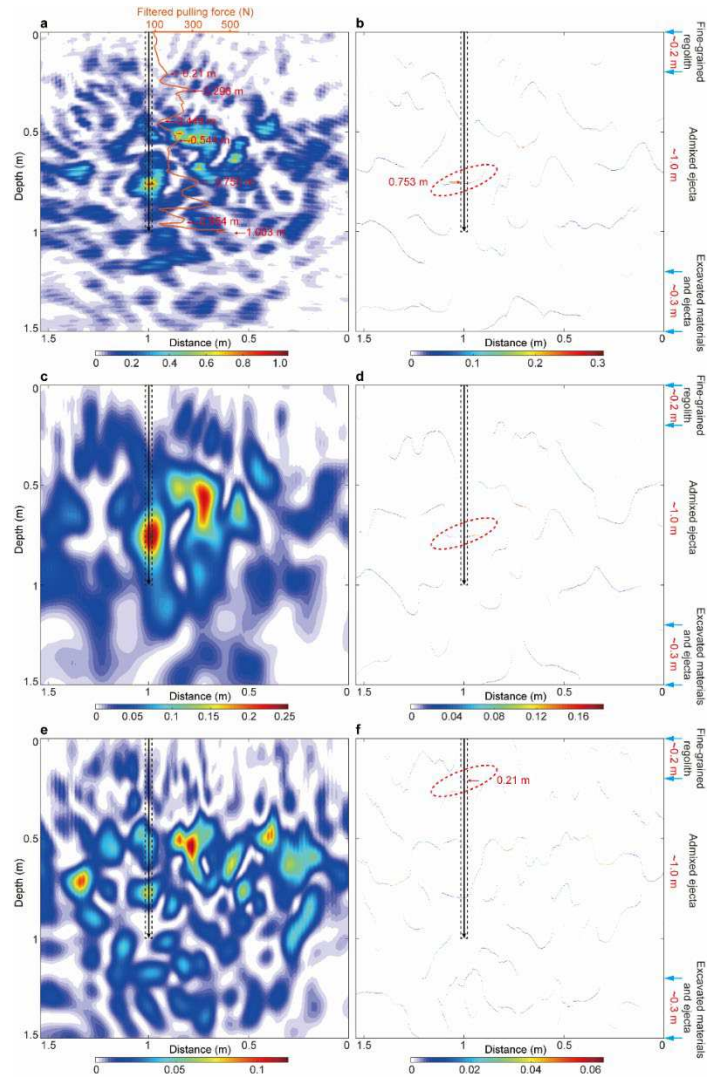
418

419 **Fig. 2 The LRPR data include 132 traces, which is sequenced according to the antenna**
420 **offsets.** The vertical axis refers to two-way travel time and the horizontal axis is the number of
421 traces. Grayscale indicate amplitudes. Pre- and post-background-removal of the LRPR data are
422 shown in Fig. 6.



423

424 **Fig. 3 LRPR data processing using the Kirchhoff migration and ridge detection method**
 425 **within ~4.5 m of burial depth. a** Kirchhoff migration on recovering the true depths and shapes
 426 of the subsurface structures. Signals envelopes were calculated using the Hilbert transform along
 427 depths, which are used to unravel lunar regolith thickness and structures. **b** Improved LRPR data
 428 from time-frequency slices at the central frequency after ridge detection. Black dotted lines
 429 represent the drilling location and the red dotted line represents the depth of obstacles
 430 encountered while drilling (~0.75 m). Black arrows indicate the main delamination position of
 431 units A-D and the blue arrows indicate the detailed delamination position in unit A.



432

433 **Fig. 4 Time-Frequency division results of the processed LRPR data using the Kirchhoff**

434 **migration and ridge detection method within ~1.5 m. a and b Detailed structures within depth**

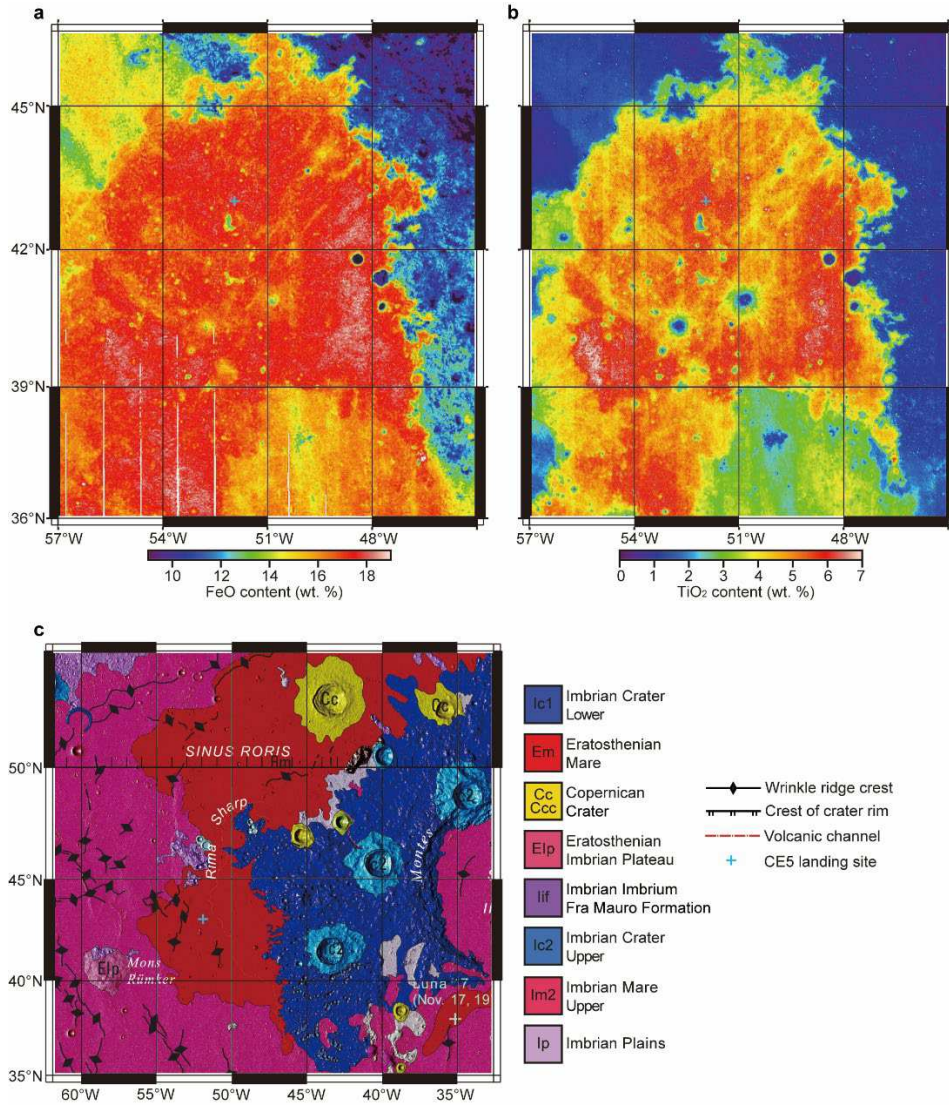
435 **of 1.5 m. The orange curve represents the pulling force curve using a low-pass filter, which**

436 **remains several main force positions. The red arrows indicate the large force feedback positions**

437 **(e.g. 0.753 m). c and e Signals along the depth direction were decomposed into low and high**

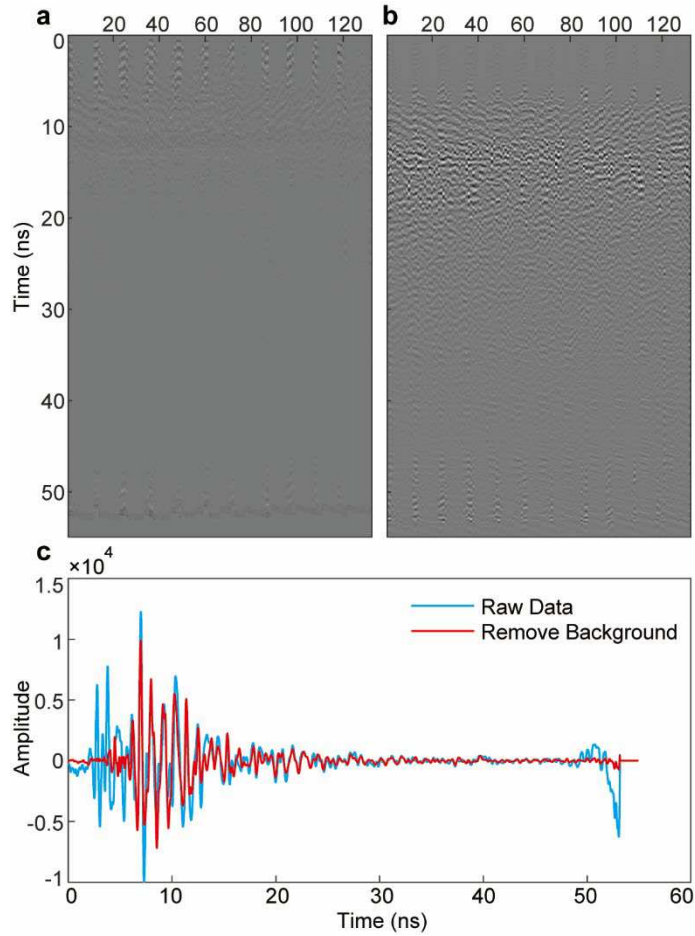
438 **frequency bands using bandpass filtering. d and f the corresponding LRPR data after ridge**

439 **detection.**



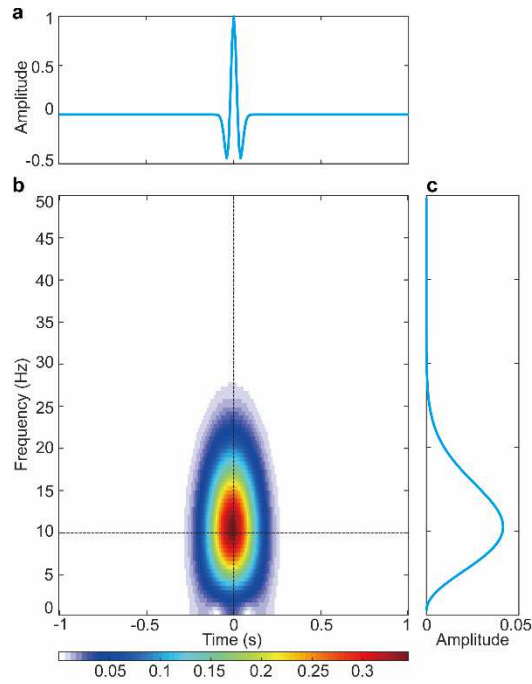
440

441 **Fig. 5 a FeO content, b TiO₂ content and geological map around the CE-5 landing site in the**
 442 **northern Oceanus Procellarum. The CE-5 landing site belongs to the eastern mare unit, which**
 443 **has high FeO and TiO₂ contents.**



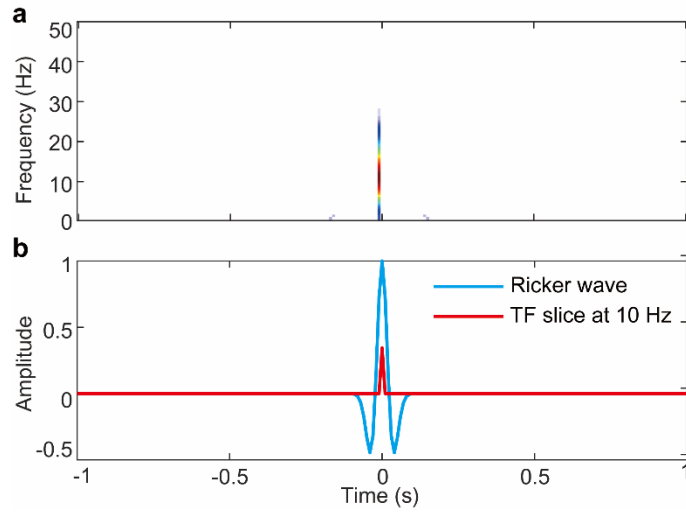
444

445 **Fig. 6 The LRPR data processing.** **a** The original 132 traces of LRPR data sequenced according
 446 to the antenna offsets. **b** Pre-processing results of the LRPR data. Processing procedures include
 447 DC removal, cable delay correction, and background removal. **c** Comparison of the influence of
 448 background removal on LRPR data preprocessing.



449

450 **Fig. 7 The STFT processing of a simulated Ricker wave.** a The time-series waveform of a
 451 simulated Ricker wave. b Time-frequency representation of the signal generated by STFT. c The
 452 frequency spectrum of the signal. The STFT has the capacity to expand one-dimensional signals
 453 into two-dimensional time-frequency domain. However, the time-frequency energy has a large
 454 distribution, which has negative effect to determine accurate travel time of the reflected
 455 electromagnetic waves.



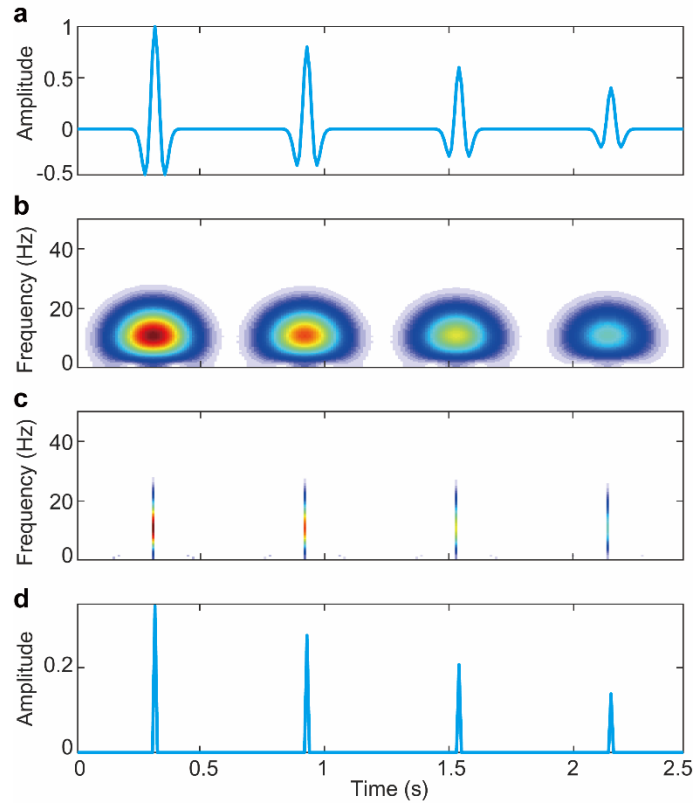
456

457 **Fig. 8 Ridge detection processing.** **a** The time-frequency representation using ridge detection. **b**

458 The time-frequency slice at the central frequency point compared to the original Ricker wave.

459 The time-frequency representation after ridge detection has a highly energy concentrated

460 distribution, which can be used to abstain the precise travel time of the Ricker wave.



461

462 **Fig. 9 Ridge detection processing for a simulated multi-component signal.** **a** A simulated
 463 time-series signal consisting of four Ricker waves. **b** The time-frequency representation generated
 464 by STFT. **c** The time-frequency representation after ridge detection. **d** The time-frequency slice at
 465 the central frequency point. This simulation further confirms that the concentrated time-frequency
 466 representation has better capacity to determine the precise travel time of the Ricker wave.